Journal of Geophysical Research: Space Physics

RESEARCH ARTICLE
10.1002/2017JA025141

Diurnal Variations in Global Joule Heating Morphology and Magnitude Due To Neutral Winds

D. D. Billett[1], A. Grocott[1], J. A. Wild[1], M.-T. Walach[1], and M. J. Kosch[2]

[1]Physics Department, Lancaster University, Lancaster, UK, [2]South African National Space Agency, Hermanus, South Africa

Key Points:
- We derive statistical patterns of high-latitude Joule heating for varying universal times
- Joule heating has a significant universal time dependence due to varying neutral winds
- Season and level of geomagnetic activity affect how much of a contribution the neutrals make

Correspondence to:
D. D. Billett,
d.billet@lancaster.ac.uk

Citation:
Billett, D. D., Grocott, A., Wild, J. A., Walach, M.-T., & Kosch, M. J. (2018). Diurnal variations in global Joule heating morphology and magnitude due to neutral winds. *Journal of Geophysical Research: Space Physics*, *123*, 2398–2411. https://doi.org/10.1002/2017JA025141

Received 19 DEC 2017
Accepted 27 FEB 2018
Accepted article online 5 MAR 2018
Published online 30 MAR 2018

Abstract In the polar ionosphere, variations in Joule heating are significantly controlled by changes in plasma convection, such as that brought about by changes in the interplanetary magnetic field. However, another important consideration when calculating Joule heating is the velocity difference between this plasma and the neutral thermosphere colocated with the ionosphere. Neutral wind data are often difficult to obtain on a global scale; thus, Joule heating has often previously been calculated assuming that neutral velocities are small and can therefore be neglected. Previous work has shown the effect of neutral winds on Joule heating estimations to be more significant than originally thought; however, the diurnal variations of the neutrals due to changes in solar pressure gradients and Coriolis forces have yet to have their impact on Joule heating assessed. We show this universal time effect to be significant in calculating Joule heating and thus can differ significantly from that calculated by neglecting the neutrals. In this study, we use empirical models for the neutral wind, conductivities, and magnetic field to create Northern Hemispheric patterns of Joule heating for approximately 800,000 individual plasma convection patterns generated using data from the Super Dual Auroral Radar Network. From this, a statistical analysis of how Joule heating varies in morphology and magnitude with universal time is shown for differing seasons and levels of geomagnetic activity. We find that neutral winds do play a significant role in the morphology and total energy output of Joule heating.

1. Introduction

Joule Heating in the ionospheric *E* and *F* regions is a significant energy sink of magnetosphere-ionosphere coupling, arising due to the exchange of momentum between constituent charge carriers and neutrals. Joule heating has been estimated to account for up to 70% of the total ionospheric power input during geomagnetic storms (Knipp et al., 2004). Heating effects can cause perturbations of the upper thermosphere (Huang et al., 2012) as well as changes to general atmospheric composition that can impact low Earth orbiting satellites (Tsurutani et al., 2004). It is therefore important to be able to accurately calculate Joule heating rates.

The morphologies of the ionospheric plasma convection and neutral atmospheric winds are both heavily studied areas. At polar (>60° magnetic latitude) *F* region altitudes of about 250 km, ion motion is controlled primarily as a result of the solar wind interaction with the Earth's magnetosphere, opening and closing flux at the dayside and nightside magnetopause (Cowley & Lockwood, 1992; Dungey, 1961). Neutral winds, however, are driven by a combination of ion-neutral drag, Coriolis forces, and solar pressure gradients (Rishbeth, 1977). As a result of the influence of ion-neutral drag, a common neutral wind pattern exists which is close in morphology to the prevailing ionospheric convection pattern (Sakanoi et al., 2002; Tsuda et al., 2007). Ion-neutral drag produces regions where the ion and neutral trajectories align, leading to lower relative velocities and thus low Joule heating. Coriolis forces, solar pressure gradients, and other forces deviate the neutrals from that alignment, resulting in larger relative velocities and increased Joule heating.

Plasma convection is most typically centered about the geomagnetic pole, with the dayside cusp located somewhere around magnetic local noon (Crooker, 1979). For the case of steady solar wind driving conditions, whereby a convection pattern does not change much over the course of a day, varying pressure gradients due to the magnetic pole rotating in and out of sunlight acts to force neutrals away from regions of increased temperatures (Liu et al., 2006; Titheridge, 1995). This means that the neutral wind pattern with respect to the magnetic latitude, magnetic local time coordinate system (MLAT-MLT) is changing while the convection remains relatively unchanged. Joule heating therefore also changes in this scenario. In the forthcoming

sections, we consider these particular conditions and examine the universal time (UT) dependence of Joule heating due to the regular, diurnal variations of the neutral wind.

The rate of Joule heating in a medium is calculated as the dissipation rate of perpendicular currents, $\mathbf{J}_\perp \cdot \mathbf{E}$ (Lu et al., 1995). This is given by

$$\mathbf{J}_\perp \cdot \mathbf{E}_{\text{total}} = \sigma_P \left(\mathbf{E} + \mathbf{V_n} \times \mathbf{B}\right)^2 \tag{1}$$

where $\mathbf{E}$ is the convection electric field, σ_p is the conductivity in the direction of the electric field (Pedersen), and $\mathbf{V_n} \times \mathbf{B}$ accounts for the electric field generated by the neutral wind dynamo due to the drag imposed on the charged ionosphere. Although it is assumed that Joule heating is deposited over a range of altitudes (mostly under 150 km, Huang et al., 2012), it was shown by Lu et al. (1995) that the entire ionospheric height-integrated effective pattern of neutrals is approximately equal to those seen at 160 km. If we therefore assume that all parameters remain constant over an altitude range where Joule heating is being deposited, then the height-integrated Joule heating rate, given by J. Baker et al. (2004), is

$$\Sigma Q_j = \underbrace{\Sigma_p E^2}_{Q_c} + \overbrace{\underbrace{2\Sigma_p \mathbf{E} \cdot \left(\mathbf{V_n} \times \mathbf{B}\right)}_{Q_w} + \Sigma_p \left(\mathbf{V_n} \times \mathbf{B}\right)^2}^{Q_{w2}}}^{Q_{w1}} \tag{2}$$

where Σ_P is the height-integrated Pedersen conductivity. Q_c is known as the convection heating, which is the energy contributed from plasma convection against a zero neutral velocity background. In the case of the static MLAT-MLT convection pattern described above where $\mathbf{E}$ remains steady, the value of the convection heating term would only be controlled by any changes in Pedersen conductivity. Q_w is known as the wind correction term and includes two components: one which accounts for the direction of the neutrals relative to the plasma (Q_{w1}) and one that describes heating due to neutrals moving against motionless plasma (Q_{w2}). Q_{w1} can be negative if the neutrals and plasma flow in the same direction, meaning Q_w itself can also be negative and thus reduce the heating given by Q_c alone. Often, contributions from neutral winds have been neglected because Q_c is usually much greater than Q_w (Crowley & Hackert, 2001; Matsuo et al., 2003), while other studies have shown that the neutrals, and thus Q_w, can effect Joule heating more substantially (Deng & Ridley, 2007; Lu et al., 1995; Thayer, 1998).

Simultaneous measurements of all parameters required to calculate Joule heating with a large enough spatial coverage is difficult; therefore, previous studies have included estimations based on geomagnetic indices (Baumjohann & Kamide, 1984; Lu et al., 1998), incoherent and coherent scatter radar measurements (Aikio & Selkälä, 2009; Cai et al., 2016; Kosch & Nielsen, 1995), and empirical models (Dickinson et al., 1981; Weimer, 2005). The Super Dual Auroral Radar Network (SuperDARN) can offer high spatial-temporal resolution global maps of convection electric fields (Chisham et al., 2007), although neutral winds and conductivities are much more difficult to measure on a similarly large scale. Global estimations of these parameters have therefore utilized the averaging of large data sets consisting of satellites and ground-based radars. Thayer and Killeen (1993), Lühr et al. (2007), and Förster et al. (2008) derived statistical patterns for the neutral winds, which revealed a near-similar structure to a typical two-cell plasma convection pattern (antisunward flow across the magnetic polar cap and return flow at dusk MLT). All, however, found several divergences from plasma convection in the patterns due to Coriolis forces and pressure gradients such as the persistent absence of a neutral wind dawn cell. A limitation of these models is also that they are averaged over all universal times and thus provide no temporal information. We instead utilize the Horizontal Wind Model 14 (HWM14) (Drob et al., 2015) for the neutral winds, which does include temporal variability. Additionally, we use statistical models (Hardy et al., 1987; Rich et al., 1987) for the Pedersen conductivity and the International Geomagnetic Reference Field (IGRF), 12th generation (Thébault et al., 2015), for the magnetic field.

2. Data

2.1. Neutral Winds

HWM14 is an empirical model of neutral wind velocities from the ground to approximately 600 km in altitude. It uses statistical averages from numerous ground-based and satellite data sets to create wind patterns with input parameters of UT, day of the year, geomagnetic *Ap* index, altitude, and geographic latitude/longitude. As stated previously, studies have used 160 km as an altitude to assess neutral winds due to this being

representative of the total ionosphere height-integrated winds. We therefore use the same reasoning by assessing HWM14 at 160 km for this study.

There is an ion-neutral drag time lag between the plasma convection and the neutral winds such that large changes in convection will not be immediately visible in the neutrals until after some time. The neutral wind reaction time has been measured previously within the order of minutes to hours (Deng et al., 2009; Kosch et al., 2001). However, HWM14 is not a global circulation model and therefore has no memory of previous conditions. This means that during periods where the plasma velocities change, HWM14 will incorrectly represent the contribution of the neutral winds to Joule heating calculations after a time frame where the neutrals should have responded to ion-neutral drag effects. HWM14 neutral wind patterns are calculated based on *Ap* index-binned averages for a certain time rather than direct ion-neutral drag derivations from an ionospheric convection pattern. If, however, it is assumed that a convection pattern with a corresponding *Ap* has been steady for a sufficiently long enough time, the neutrals will have spun up into some equilibrium morphology with regard to ion-neutral drag. HWM14 therefore creates a reasonably representative climatological wind pattern for a specific *Ap* index at some UT on average.

The neutral wind flywheel effect (W. Deng et al., 1993) is another phenomena of the thermosphere which effects the morphology of the plasma convection. At high latitudes, the neutral wind dynamo in general is not as significant as it is at middle and lower latitudes due to the dominance of the convection electric field (Richmond & Roble, 1987). However, under situations whereby a sustained convection electric field changes suddenly, such as due to changes in the interplanetary magnetic field (IMF), then the neutrals will continue to move at a lagged morphology until they have fully responded to ion-neutral drag. During this time, the neutral winds can drive significant current systems and even impose drag forces on the plasma. In this case, HWM14 would accurately represent a lagged neutral wind when accompanied with accurate plasma data for the duration of which the *Ap* index does not change.

2.2. Electric Field

The SuperDARN (Chisham et al., 2007) is a network of over 30 radars measuring the line-of-sight component of *F* region $\mathbf{E}\times\mathbf{B}$ ion velocities of convective plasma, among other parameters. The motions of these convective ions can equivalently be represented by contours of constant electrostatic potential via consideration of the electric field, given by

$$\mathbf{E} = \nabla\Phi \tag{3}$$

and

$$\mathbf{v} = \frac{\mathbf{E}\times\mathbf{B}}{B^2} \tag{4}$$

where Φ is the electrostatic potential and $\mathbf{v}$ is the plasma velocity, by using the map potential technique described by Ruohoniemi and Baker (1998). In this case, the convection electric field is derived from the fitting of a spherical harmonic expansion of the ionospheric electrostatic potential to the measured line-of-sight velocities available from the SuperDARN network. A background empirical model, which varies depending on IMF components in the geocentric solar magnetospheric (Hapgood, 1992) *Y*-*Z* plane (otherwise known as clock angle), is used to constrain the fitting in regions of limited radar data coverage.

2.3. Pedersen Conductivity

Pedersen conductivities were calculated from two models, which account for the largest contributions (Rich et al., 1987). These contributions are from solar extreme. The solar EUV component (Σ_P^{Sun}) has been shown to be well represented as a function of the solar zenith angle, χ, and the 10.7 cm radio flux intensity, $f_{10.7}$ (Kamide & Matsushita, 1979; Rich et al., 1987; Wallis & Budzinski, 1981):

$$\Sigma_P^{\mathrm{Sun}} = 12.5\left(\frac{f_{10.7}}{180}\right)^{\frac{1}{2}}\frac{0.06+\exp\left[1.803\tanh\left(3.833\cos\chi\right)+0.5\cos\chi-2.332\right]}{\left[1-0.99524\sin^2\left(\lambda_{\mathrm{ss}}\right)\right]\times\left[1+0.3\cos^2\left(\lambda_{\mathrm{ss}}\right)\right]} \tag{5}$$

where λ_{ss} is the colatitude of the subsolar point. The numerator of the second term simply describes the decrease in conductivity with increasing solar zenith angle across the day-night terminator. The denominator of the same term is the adjustment in latitude for the position of the subsolar point. In the magnetic pole-centered coordinate system, there is a UT variation due to the offset with respect to the geographic spin axis, creating a 24-hr cycle of enhanced and suppressed solar EUV conductance. This is because of the variation

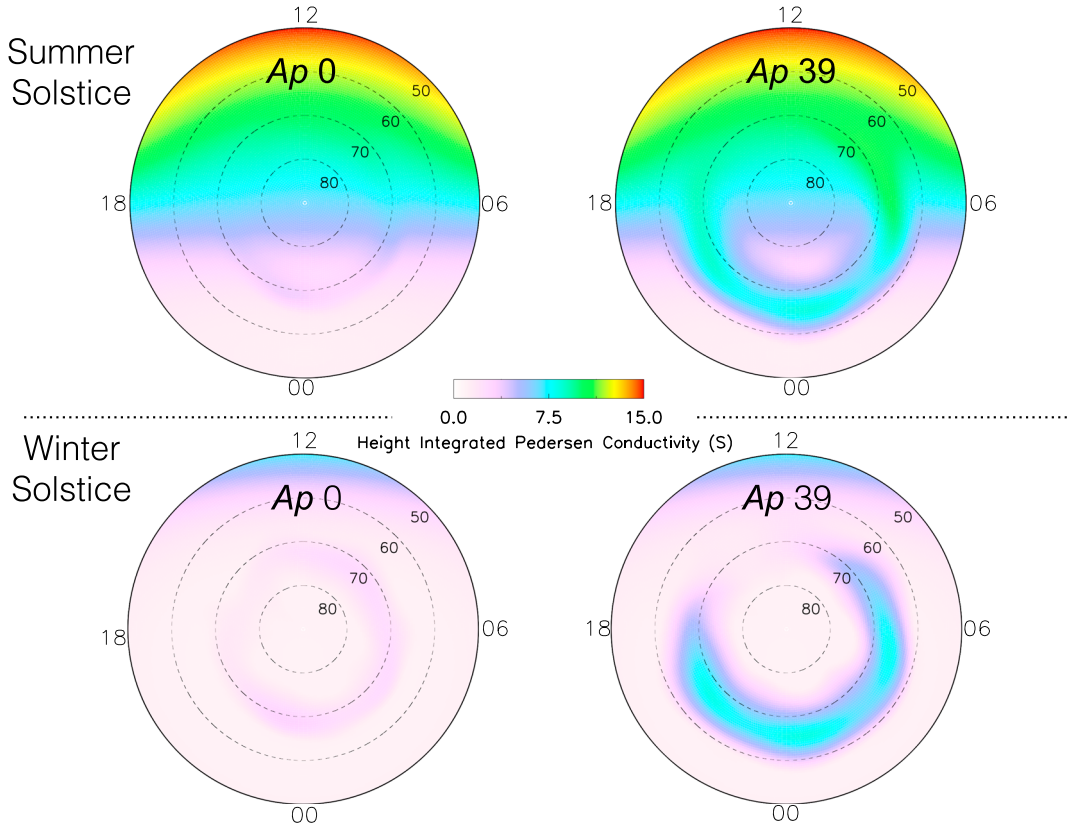

Figure 1. A comparison of height-integrated Pedersen conductivities for Northern Hemisphere summer and winter times with *Ap* indices of 0 and 39, at 00 universal time. The plots are in updated altitude adjusted corrected geomagnetic latitude, magnetic local time coordinates (Baker & Wing, 1989; Shepherd, 2014) extending to 50° magnetic latitude. $f_{10.7}$ is a constant 226 solar flux units for all plots.

in the angle between the Earth's magnetic pole and the subsolar point, otherwise known as the dipole tilt angle (Laundal & Richmond, 2017). Additionally, there is a large seasonal difference in dipole tilt ranges at polar latitudes, which can bring about significant variation in Joule heating between the hemispheric summer and winter months.

Some optical instruments (such as Global Ultraviolet Imager aboard Thermosphere Ionosphere Mesosphere Energy and Dynamics) are able to infer the height-integrated Pedersen conductivity due to particle precipitation (Σ_P^{Aurora}) from measurements of auroral energy (E_0) and energy flux (I) (Baker et al., 2004; Hardy et al., 1987; Robinson et al., 1987) through the empirical relation:

$$\Sigma_P^{\text{Aurora}} = \left[\frac{40E_0}{(15 + E_0^2)}\right] I^{0.5} \tag{6}$$

however, these parameters are usually not available with large enough spatial and temporal coverage to perform effective global-scale studies. Kosch et al. (1998) showed that all-sky images can be used to calculate the Pedersen conductivity from 557.7 nm auroral emissions, but this would only provide coverage that was limited to the field of view of the instrument. Hardy et al. (1985, 1987) developed statistical averages of auroral precipitation patterns from the Defense Meteorological Satellite Program and Solwind satellites based on *Kp* index, of which an estimated height-integrated Pedersen conductivity could be calculated using the relationship in equation (6). Small-scale conductivity enhancements of the order of about half a degree in longitude, which can vary greatly from the statistical average, are lost in this process.

Because the two height-integrated conductivity models discussed are considered to overlap completely in altitude, we may not simply add them. This is due to the particle precipitation model intrinsically containing

information about the solar EUV component at auroral oval locations. A root-sum-square approximation is therefore used, which has been shown to produce the lowest deviation from measurements (Wallis & Budzinski, 1981). The total height-integrated Pedersen (Σ_P) conductivity for a specified position is thus a function of $f_{10.7}$, χ, and *Kp* index (which has a direct translation to *Ap*, Clúa de Gonzalez et al., 1993):

$$\Sigma_P = \sqrt{\left(\Sigma_P^{\text{Sun}}\right)^2 + \left(\Sigma_P^{\text{Aurora}}\right)^2} \tag{7}$$

Figure 1 shows how global conductivity patterns change due to season and *Ap* index using these two models. Σ_P weights total convection heating rates, resulting in a greater Q_c during the summer months and UT's where the magnetic polar cap is more sunlit (Σ_P^{Sun} controlled). More geomagnetically active times also cause an enhanced Q_c where the precipitation conductivity oval extends to lower latitudes (Σ_P^{Aurora} controlled). Solar EUV radiation is the dominant source of conductivity during hemispheric summer months, but not in winter. Electron precipitation conductivities are invariant with season using these models.

2.4. Magnetic Field

The IGRF 12th generation (Thébault et al., 2015) is used to model the Earth's tilted dipole field as a function of geographic position, time, and altitude. The magnitude of **B** over the limited altitude range assumed in equation (2) does not vary substantially; therefore, an altitude of 160 km was used to match that used in HWM14. At the high magnetic latitudes used in this study, the terrestrial field is mostly vertical and does not vary much, therefore not contributing substantially to any Joule heating variability unless geomagnetically disturbed.

3. Method

Joule heating was initially calculated using a database of every Northern Hemispheric convection electric field pattern, integrated over a period of 2 min each, generated using SuperDARN data and the map potential technique from 2000 to 2006, as well as the other sources of data described in section 2. To ensure that patterns used contained enough data to warrant a realistic map potential model output and lower the dependence on the map potential model, a quality threshold of 200 SuperDARN velocity vectors was used for each individually generated SuperDARN convection pattern. This was found to reduce the number of Joule heating patterns that were used by approximately 55% to around 800,000. The electric field, Pedersen conductivity, neutral wind, and magnetic field were each interpolated on to an equal area polar grid, centered on the magnetic pole and fixed in MLT. Grid cells extend 1° wide in magnetic latitude ranging from 50° to 90°, with a variable longitude/MLT width with increasing latitudes. This maintains an equal area resolution over the entire grid. The result is one Joule heating pattern for every SuperDARN convection pattern used. It should be noted that a blanket threshold of 200 SuperDARN velocity vectors does not imply an even spatial coverage across all local times. Multiple radars are, however, required to achieve this many vectors in one map, improving this to some degree.

Joule heating has a dependence on season due to the solar EUV conductivity component, so it is an important influence to consider when looking at diurnal variations. The same can be said about the morphology and magnitude of the electric field with varying geomagnetic activity (Ahn et al., 1992). To capture both of these, as well as any trends due to UT, all Joule heating patterns are binned first into two seasons representing the Northern Hemispheric light (1 April to 30 September) and dark (1 October to 31 March) months. From here, patterns are additionally binned into three ranges of *Ap* index representing geomagnetically low (0–6), moderate (7–22), and high (27–400) activity levels. Finally, the patterns are binned into 24 evenly spaced UT hourly ranges (0–23). Histograms of the counts in each of these bins are shown in Figure 2.

Ap index-based bins were chosen for our analysis for consistency with the HWM14. It should be noted that this does not allow for a full analysis of plasma convection, which is controlled by factors such as the IMF clock angle. Although we expect *Ap* to respond to changes in the IMF over long (>3 hr) timescales, there is not necessarily a one-to-one relationship between any given IMF magnitude or direction and the associated *Ap* index.

In order to keep the quantity of Joule heating patterns in each bin high, seasonal analysis was restricted to light and dark months, as defined above. Similarly, ranges of *Ap* indices were chosen such that there would be enough data in each UT bin, representing low, moderate, and high geomagnetic activity periods, respectively. It is noted that the higher activity bin (*Ap* indices 27–400) contains consistently lower numbers

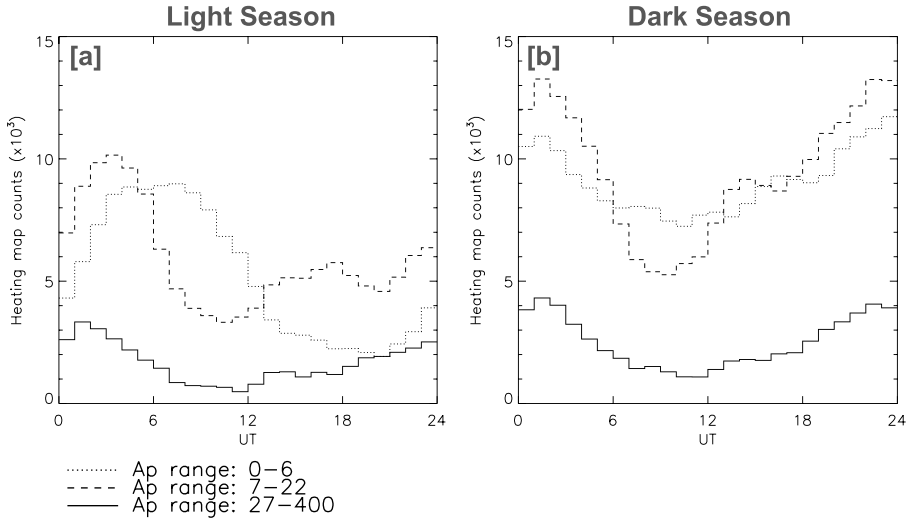

Figure 2. The number of Joule heating maps in each universal time bin described in section 3 for the Northern Hemispheric (a) light and (b) dark seasons. The 27–400 *Ap* range has consistently the lowest number of counts per bin, and all counts increase for the dark season.

of Joule heating patterns in each UT bin than the other ranges. This is due to the occurrence of *Ap* indices decreasing substantially at higher activity levels. It was decided to not decrease the lower bound of this *Ap* bin to include more data, as the result would have weighted this bin too heavily toward lower geomagnetic activity levels.

4. Results and Discussion

As an initial visualization, Figure 3 shows MLAT-MLT plots of Q_c, Q_w, and total Joule heating (Q_J) for 00 UT, 06 UT, 12 UT, and 18 UT for the moderate *Ap* index range (7–22) during the light season. We can immediately see that changes in the diurnal conductivity at the magnetic pole mean Q_c is largest when the polar cap is most sunlit.

Considering the heating due to Q_c in Figure 3, enhancements are mainly confined to the regions where the gradient of electric potential (i.e., the electric field, **E**) is usually steepest. This is typically at the 60–75° MLAT dusk and dawn sunward convection regions. Q_c will also be greater on the dayside due to higher solar EUV Pedersen conductivity. UT variations only arise due to changes in this conductivity which is dependent on the dipole tilt angle, which causes a larger magnitude of Q_c globally at 18 UT. This is consistent with the offset of the geomagnetic pole from geographic, which is approximately 5 hr in longitude and thus introduces a conductivity peak at approximately 17 UT instead of 12 UT. Note that in the region of the auroral oval, conductivity is also enhanced, so this will increase Q_c in the presence of strong electric fields.

Changes in the magnitude of Q_w with UT are also produced by conductivity changes. The largest single positive and negative values of Q_w therefore occur at 18 UT. Regions of wind heating ($+Q_w$) occur when neutrals directionally oppose the ions, which on average happens consistently in the dawn sector. Reductions in heating relative to Q_c ($-Q_w$) occur when the ions and neutrals align in the same direction, which primarily happens in the dusk sector and high magnetic latitude (>80°) regions. This implies that the duskside neutral wind pattern tends to align more closely with the plasma convection than the dawnside pattern. Dusk and dawn asymmetry in neutral winds has been observed before in satellite measurements (Dhadly et al., 2017; Förster et al., 2008; Lühr et al., 2007), global circulation model observations (Deng & Ridley, 2006), and single radars (Baron & Wand, 1983), appearing more prominently at higher levels of geomagnetic activity. A dusk cell is also consistently visible in HWM14, while a dawn cell is rarely, if ever, seen to form. This is attributed to Coriolis and centrifugal forces (Fuller-Rowell & Rees, 1984) and means that under most geomagnetic conditions, there is a tendency for greater Joule heating in the dawn sector, which is consistent with previous studies (Deng & Ridley, 2007; Matsuo et al., 2003; McHarg et al., 2005; Thayer et al., 1995). The morphology of Q_w also changes

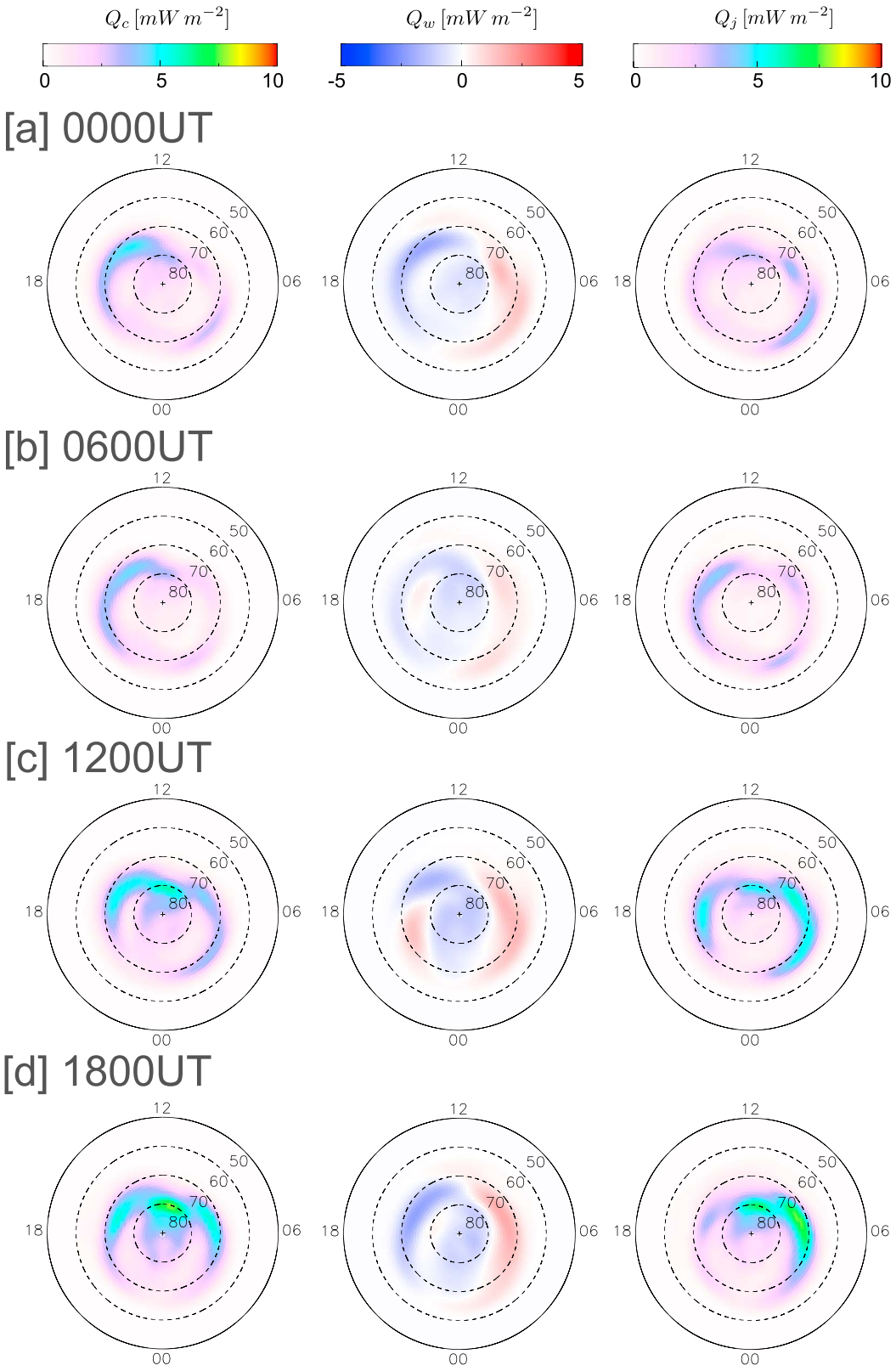

Figure 3. Light season convection heating (Q_c, left column), wind correction (Q_w, middle column), and Joule heating (Q_j, right column) patterns for *Ap* range 7–22 for (a) 00 universal time (UT), (b) 06 UT, (c) 12 UT, and (d) 18 UT. Plots are the same format as Figure 1.

with UT in a way that is distinct from the conductivity cycle. This is shown most clearly by the duskside Q_w change from negative to positive between 06 UT and 12 UT, indicating that the neutral wind pattern is changing with respect to plasma convection as UT progresses.

The sum of Q_c and Q_w gives the total Joule heating (Q_j), also shown in Figure 3. Q_j is mostly reduced from Q_c on the duskside and enhanced from Q_c on the dawnside, at all UTs, in accordance with the wind correction. Dawnside Q_j is lowest at 06 UT, while the maximum is at 18 UT, both corresponding to times of low and high conductivity, respectively (as can be seen in the equivalent Q_c patterns). The minimum and maximum duskside Q_j, however, does not correspond to the minimum and maximum in conductivity levels, occurring at 00 UT and 12 UT respectively, due to the neutral wind directional changes with UT mentioned previously. Overall, Joule heating is much more spatially variable in MLT than the convection heating because of the UT dependence in the wind correction.

To capture the full UT dependence of Joule heating morphology for both light and dark seasons, as well as the three *Ap* index ranges, heating averages for each hour MLT sector of each pattern were derived and plotted with respect to the 24 UT bins that are shown in Figure 2. This gives one 24 × 24 pixel plot per geomagnetic activity range, per season for Q_c, Q_w, and Q_j. Magnetic latitudes greater than 80° and less than 60° were not considered in averaging because those regions either have a statistically uniform distribution of Joule heating, or no heating. The results are shown in Figure 4. For Q_c and Q_j, a black cross was placed in the MLT sector where the highest average heating occurred to better track morphology changes.

For all Q_c plots, heating is mostly confined to the predusk sector, extending closer to noon at higher activity level ranges. The maximum Q_c stays primarily on the duskside at all UTs, although is more spatially variable in MLT during the dark season and can be located on the dawnside at later UTs. All regions of Q_c become more prominent at approximately 17 UT, which corresponds to the peak in solar conductivity that can also be seen in Figure 3. The largest values of Q_c occur in Figure 4c, which is expected due to high solar conductivity and large convection electric fields that are associated with high geomagnetic activity (Ahn et al., 1992).

During the dark season, the magnitude of Q_c is lower and there is also more variability in the location of maximum heating. This stays mostly close to dusk but becomes sporadic in Figure 4f. This could be an indication of lower data coverage, or greater morphological variability in the convection electric field during active periods and dark months. The latter suggestion agrees with the conclusions made by Matsuo et al. (2003) and Pettigrew et al. (2010) that the reconnection topology might vary with changing solar induced conductivity, thus affecting the convection morphology.

As discussed previously, HWM14 shows asymmetry between dusk and dawn neutral winds, leading to increased Joule heating on the dawnside. This is shown by the constantly positive dawnside Q_w for all plots in Figure 4. Q_w is mostly negative on the duskside, apart from a range of UTs centered around 12 UT which turn positive. This range reduces slightly with increased geomagnetic activity levels. As in Figure 3, this indicates that on average, neutrals typically flow in the direction of the plasma on the duskside, while the opposite is true for the dawnside. The change from negative to positive on the duskside must be due to UT variations in the relative neutral-ion morphologies. Q_c plots show that for the most part the convection electric field only varies on the dusk side due to solar conductivity enhancements when considering the statistical patterns presented here. This means that the neutral wind morphology is likely changing direction more than the plasma with UT on the duskside. This agrees with previously observed neutral wind asymmetries (Baron & Wand, 1983). It is important to note, however, that on an event-by-event basis, electric field variability can potentially contribute much more to Q_c UT variability.

As a result of Q_w, the morphology of Q_j differs significantly from Q_c. Dawnside Joule heating becomes more enhanced between 12 UT and 24 UT and increases in magnitude and UT spread with increasing geomagnetic activity. The Q_w hot spot on the duskside also causes the corresponding Joule heating peak to move closer to magnetic local midnight. This is in contrast to Q_c, for which the peak generally changes very little in MLT, apart from during the dark season high *Ap* index bin as mentioned previously (Figure 4f). This is clearest in Figure 4c due to a clear trend in maximum Joule heating migrating from about 14 MLT to 19 MLT between 00 UT and 10 UT. Due to the Q_w reductions in heating at all other UT's on the duskside, dawnside heating plays a much larger role than when considering Q_c alone.

As estimation of the total Joule heating in the Northern Hemisphere, we can calculate the area-integrated heating rates for each Joule heating pattern upwards of 50° of magnetic latitude. This was done for each hour

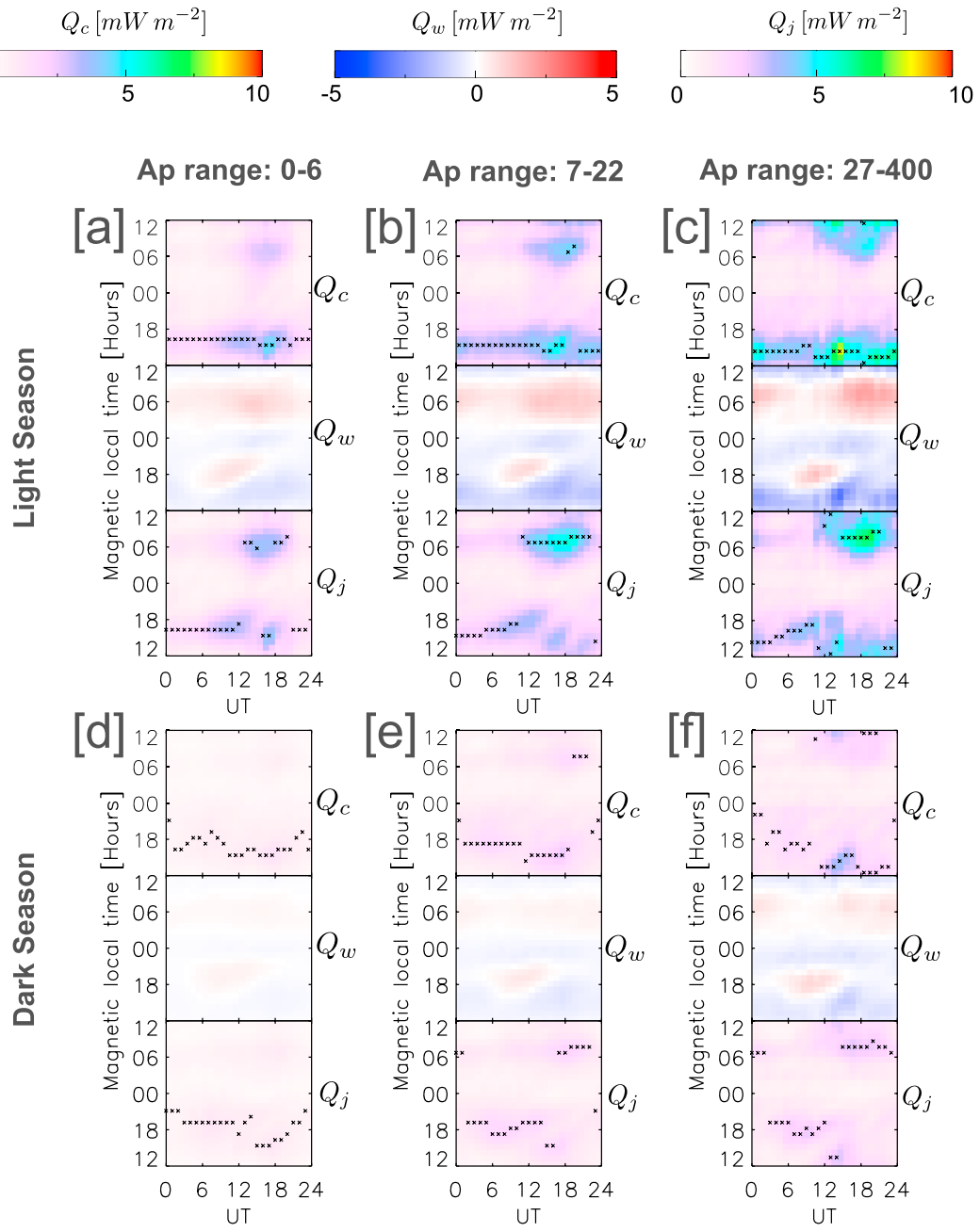

Figure 4. Magnetic local time sector averages for Q_c, Q_w, and Q_j with universal time (UT). *Ap* index ranges shown are for the light (a–c) and dark (d–f) season bins shown in Figure 2.

of UT in each *Ap* index range for both the light and dark seasons. The results showing the area-integrated Q_c, Q_w, and Q_j values ($\sum Q_c$, $\sum Q_w$, and $\sum Q_j$, respectively) are shown in Figure 5.

The most prominent feature of all $\sum Q_c$ components in Figure 5 is a diurnal cycle, mediated by the variation in solar EUV Pedersen conductivity causing increased heating at approximately 17 UT. This trend is more prominent during the light season than dark, which is reasonable because the variation of solar illumination on the summer polar cap is much greater than that on the winter. $\sum Q_c$ increases with increasing *Ap* index due to corresponding stronger electric fields and electron precipitation releated conductivity enhancements associated with high geomagnetic activity. Both Figures 5c and 5f show higher variability than the others, which is most likely due to having less data per UT bin, although the general trend is still clearly visible. It should be noted that the limited occurrence of high *Ap* index times will weigh the 27–400 bin to the lower geomagnetic

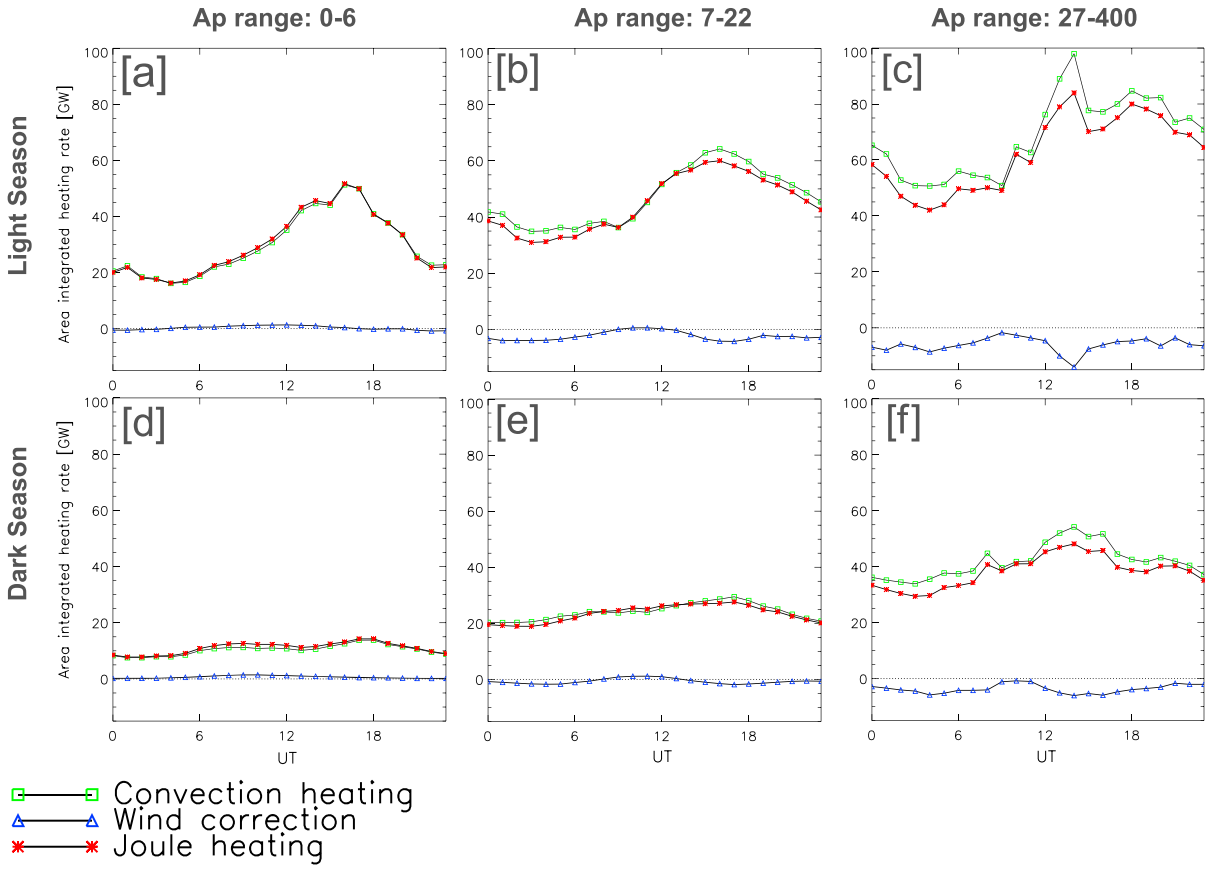

Figure 5. Area-integrated Q_c, Q_w, and Q_j heating rates with increasing universal time (UT). *Ap* index ranges shown are for the light (a–c) and dark (d–f) season bins shown in Figure 2.

activities, which will in turn weight down the area-integrated values. Therefore, we expect the $\sum Q_c$ values shown in Figures 5c and 5f to be underestimates of very active periods.

$\sum Q_w$, shows a trend which is separate from that of the solar EUV conductivity variations, displaying larger amplitudes at higher *Ap* indices. This is clearest in Figure 5b as a semidiurnal pattern which varies between a positive and negative values. This means that it is possible for the overall net contribution from the wind correction to the area-integrated Joule heating rate to be negative or positive, depending on UT. With increasing geomagnetic activity, $\sum Q_w$ is most often negative. This agrees with Lu et al. (1995) that on average, the neutral winds have a net negative effect on Joule heating with respect to convection heating.

In Figures 5c and 5f where $\sum Q_w$ is constantly negative, the semidiurnal trend still shows minima at approximately 04 UT/14 UT and maxima at 10 UT/22 UT. Before, we have seen that Q_w is mostly positive on the dawnside and negative on the duskside. This implies that the negative values for $\sum Q_w$ in Figures 5c and 5f are due to heat reductions on the duskside being larger in magnitude than the increased heating on the dawnside. This in turn indicates that neutrals tend to move in the direction of the plasma flow more at higher geomagnetic activities than lower because $\sum Q_w$ becomes increasingly negative. Considering that ion-neutral drag plays an important role in neutral morphologies, it is reasonable to assume that the increase in plasma velocity that accompanies active periods increases the drag force on the neutrals, thus forcing them into a morphology closer to that of the plasma.

The minima and maxima in $\sum Q_w$ modify $\sum Q_j$ substantially from $\sum Q_c$ at higher *Ap* indices, illustrated by the separation between the $\sum Q_j$ and $\sum Q_c$ lines. To show the proportion of the area-integrated Joule heating which is due to the wind correction, we show the percentage of $\sum Q_w$ as a proportion of $\sum Q_c$ in Figure 6. All *Ap* index ranges contain peaks in the positive direction at approximately 10 UT, which is 7 hr prior to the diurnal peak in solar conductivity seen in Figure 5. There are also troughs in the negative direction on either

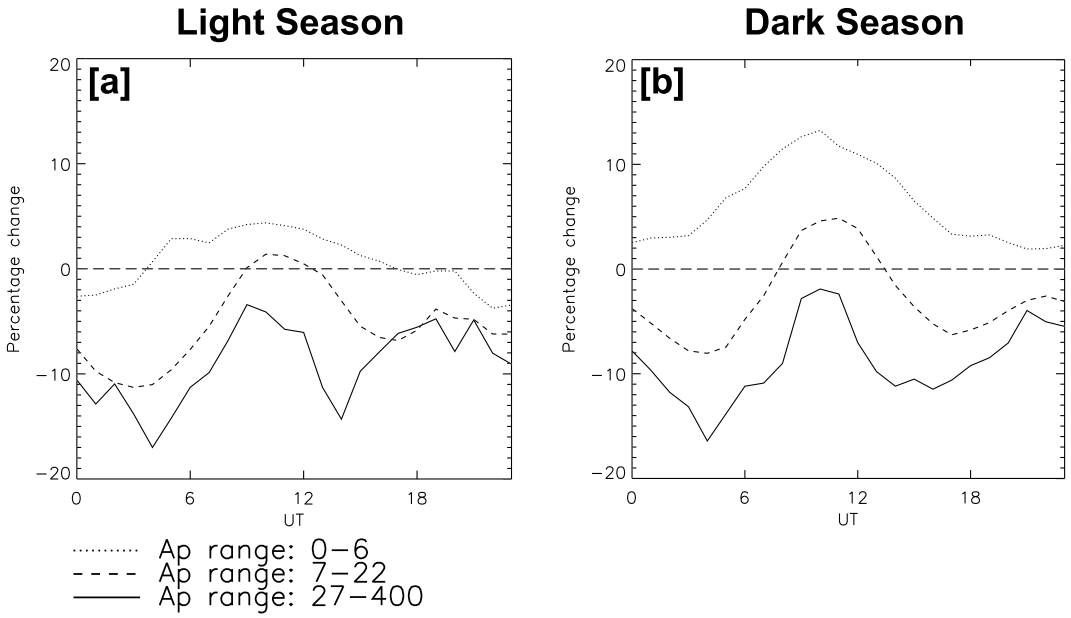

Figure 6. Percentage change in area-integrated Joule heating rate due to the area-integrated wind correction against universal time (UT). All *Ap* index ranges are shown for the (a) light and (b) dark seasons.

side of the central peak, which decrease in magnitude at times approximately before 04 UT and after 15 UT. The $\sum Q_w$ trend is otherwise diurnal in nature for the 0–6 *Ap* index range.

During the light season, the difference between the lowest and highest percentage changes due to the wind correction is 7%, 13%, and 13% for *Ap* ranges 0–6, 7–22, and 27–400, respectively. In the dark season, the percentage differences change to 10%, 13%, and 14% for the same ranges. These magnitude differences are not insignificant and demonstrate the importance of taking UT into consideration when calculating Joule heating. The tendency for the wind correction to increase heating from Q_c is also greater in the dark season than light. This is due to the large solar EUV conductivity differences between hemispheric summer and winter months. The conductivity has a large influence on the convection heating, but not as much on the wind correction, implying the magnitude of the neutral velocity with respect to the plasma convection is dictated more by changes in geomagnetic activity than season. This is almost certainly the case for the plasma convection (Ruohoniemi & Greenwald, 2005) and has also shown to be true for the neutrals (Killeen et al., 1995).

5. Summary

Approximately 800,000 SuperDARN plasma convection patterns were used together with the HWM14, IGRF, and Hardy et al. (1987) and Rich et al. (1987) conductivity models to generate statistical patterns for Joule heating, the convection heating, and wind correction, averaged in hours of UT. These were filtered additionally in order to differentiate between season and geomagnetic activity level, as both are expected to have considerable effects on Joule heating.

As the convection heating is modulated only by the Pedersen conductivity and convection electric field, the morphology remains relatively constant in the MLAT-MLT frame with UT as the variation in dipole tilt changes the magnitude for a fixed geomagnetic activity range, while the magnitude peaks at approximately 17 UT when the magnetic pole is most sunlit. Increasing geomagnetic activity is associated with stronger, more spatially equatorward convection electric fields that extend to more local times (Ahn et al., 1992); therefore, convection heating also increases and spans more local times. During the hemispheric dark months, when conductivity changes are much lower than during the light months, convection heating becomes more spatially variable, indicating some convection variability with UT.

The wind correction, which in this study is used as a measure of neutral wind influence on convection heating, has a similar morphology for both light and dark seasons and all geomagnetic activity ranges. Neutral winds consistently increase heating on the dawnside indicating they are statistically always opposing the plasma.

On the duskside, the wind correction is mostly negative, apart from during periods of UT which range from 8 to 11 hr in length during the light season and 10–15 hr in the dark season. These sign changes indicate directional changes in the neutrals with respect to the convection plasma as UT progresses, thus introducing a UT dependence to Joule heating which is separate from that induced by solar conductivity. The magnitude of the wind correction is larger at higher geomagnetic activity levels and during the light season.

Joule heating, which is the sum of the convection heating and wind correction, is affected by both in several ways:

1. The morphology of the wind correction consistently enhances Joule heating on the dawnside in agreement with several previous studies (Deng & Ridley, 2007; Matsuo et al., 2003; McHarg et al., 2005; Thayer et al., 1995). The wind correction UT dependence can either enhance or diminish Joule heating on the duskside, as well as introduce additional magnetic local time variability. If it is assumed that under steady geomagnetic activity levels, the convection electric field does not vary much spatially with UT (in the MLAT-MLT frame), then the Joule heating morphology variability must be due to neutral wind UT variability such as that brought about by Coriolis forces and solar pressure gradients. Magnetic local time averages for Q_w range between approximately −3 and 2 mW/m^2, while the corresponding Q_c can reach around 8 mW/m^2 during the sunlit months at high activity levels on average. These are, however, general underestimates of the actual peak values that both Q_w and Q_c can reach due to the spatial averaging across local time bins carried out here, as well as the weighting of the largest *Ap* index bin toward lower indices mentioned in (3).
2. Solar-induced conductivity is higher in the hemispheric light months, resulting in higher magnitudes of Joule heating. This conductivity is also at a maximum at approximately 17 UT, which coincides with a maximum dipole tilt angle toward the sun but does not necessarily coincide with maximum Joule heating in all regions due to negative wind corrections on the duskside.
3. The area-integrated (upward of 50° MLAT) wind correction rate is semidiurnal in nature. This propagates into the area-integrated Joule heating rate, which causes it to be sometimes either larger or lower than the area-integrated convection heating depending on UT. At higher levels of geomagnetic activity, the area-integrated wind correction becomes increasingly negative, meaning Joule heating no longer exceeds the value for convection heating on an area-integrated basis.
4. As a result of the diurnal variation in the area-integrated wind correction described above, the percentage contribution of the wind correction to the area-integrated Joule heating rate can vary by ±14% depending on season and geomagnetic activity level.
5. Because changes in solar EUV conductivity with season affects convection heating more than the wind correction, Joule heating in the hemispheric winter months is greater influenced by the neutral winds.

It is important to note that this method of generating statistical patterns of Joule heating does capture the increased heating due to convection electric field variability (Codrescu et al., 1995). This is because patterns of Joule heating are calculated at every SuperDARN time step instead of using statistically averaged electric fields such as that derived by Ruohoniemi and Greenwald (1996). However, the limitations of HWM14 means that the neutral atmosphere response time cannot be accounted for. The statistical Pedersen conductivity models used also do not include temporal or small scale variability, which can be significant especially at auroral latitudes (Vickrey et al., 1981). Further study will utilize high time resolution observations of neutral winds and electric fields to investigate Joule heating in comparison with the model presented here. Overall, it is clear that when considering the effect of the neutral winds on Joule heating calculations, its corresponding UT dependence can be a dominant driver of diurnal heating variations both spatialy and in magnitude.

Acknowledgments
The authors acknowledge the extensive use of data from SuperDARN, which is funded by the national funding agencies of Australia, Canada, China, France, Japan, South Africa, the United Kingdom, and the United States. SuperDARN data can be viewed online via quick-look plots or requested at the Virginia Tech SuperDARN data access portal (http://vt.superdarn.org/). The HWM14 Fortran subroutines were downloaded from the supporting information section of the corresponding article (http://onlinelibrary.wiley.com/doi/10.1002/2014EA000089/full). IGRF was used as part of the IDL Geopack DLM (http://ampere.jhuapl.edu/code/idl_geopack.html). IDL code for both conductivity models used was obtained from the Virginia Tech Data Visualisation Toolkit (DaViT) (http://davit1.ece.vt.edu/doc/overview.html). During this study, D. D. B. was supported by Lancaster University, A. G. and M.-T. W. were supported by NERC grant NE/P001556/1, and M. K. was supported by the Department of Physics and Astronomy, University of the Western Cape, Bellville, South Africa. We thank Y. Yamazaki for useful discussions regarding neutral wind and electric potential simulations.

References

Ahn, B.-H., Kamide, Y., Kroehl, H., & Gorney, D. (1992). Cross-polar cap potential difference, auroral electrojet indices, and solar wind parameters. *Journal of Geophysical Research*, *97*(A2), 1345–1352.

Aikio, A., & Selkälä, A. (2009). Statistical properties of Joule heating rate, electric field and conductances at high latitudes. *Annales Geophysicae*, *27*, 2661–2673. Copernicus GmbH.

Baker, J., Zhang, Y., Greenwald, R., Paxton, L., & Morrison, D. (2004). Height-integrated Joule and auroral particle heating in the night side high latitude thermosphere. *Geophysical research letters*, *31*, L09807. https://doi.org/10.1029/2004GL019535

Baker, K., & Wing, S. (1989). A new magnetic coordinate system for conjugate studies at high latitudes. *Journal of Geophysical Research*, *94*(A7), 9139–9143.

Baron, M. J., & Wand, R. H. (1983). *F* region ion temperature enhancements resulting from Joule heating. *Journal of Geophysical Research*, *88*(A5), 4114–4118.

Baumjohann, W., & Kamide, Y. (1984). Hemispherical Joule heating and the *AE* indices. *Journal of Geophysical Research*, *89*(A1), 383–388.

Cai, L., Aikio, A., & Milan, S. (2016). Joule heating hot spot at high latitudes in the afternoon sector. *Journal of Geophysical Research: Space Physics*, *121*, 7135–7152. https://doi.org/10.1002/2016JA022432
Chisham, G., Lester, M., Milan, S. E., Freeman, M., Bristow, W., Grocott, A., et al. (2007). A decade of the Super Dual Auroral Radar Network (SuperDARN): Scientific achievements, new techniques and future directions. *Surveys in Geophysics*, *28*(1), 33–109.
Clúa de Gonzalez, A. L., Gonzalez, W. D., Dutra, S. L., & Tsurutani, B. T. (1993). Periodic variation in the geomagnetic activity: A study based on the *Ap* index. *Journal of Geophysical Research*, *98*(A6), 9215–9231.
Codrescu, M., Fuller-Rowell, T., & Foster, J. (1995). On the importance of *E*-field variability for Joule heating in the high-latitude thermosphere. *Geophysical Research Letters*, *22*(17), 2393–2396.
Cowley, S., & Lockwood, M. (1992). Excitation and decay of solar wind-driven flows in the magnetosphere-ionophere system. *Annales Geophysicae*, *10*, 103–115. Copernicus.
Crooker, N. (1979). Dayside merging and cusp geometry. *Journal of Geophysical Research*, *84*(A3), 951–959.
Crowley, G., & Hackert, C. L. (2001). Quantification of high latitude electric field variability. *Geophysical research letters*, *28*(14), 2783–2786.
Deng, W., Killeen, T., Burns, A., Roble, R., Slavin, J., & Wharton, L. (1993). The effects of neutral inertia on ionospheric currents in the high-latitude thermosphere following a geomagnetic storm. *Journal of Geophysical Research*, *98*(A5), 7775–7790.
Deng, Y., & Ridley, A. (2006). Dependence of neutral winds on convection E-field, solar EUV, and auroral particle precipitation at high latitudes. *Journal of Geophysical Research*, *111*, A09306. https://doi.org/10.1029/2005JA011368
Deng, Y., & Ridley, A. J. (2007). Possible reasons for underestimating Joule heating in global models: E field variability, spatial resolution, and vertical velocity. *Journal of Geophysical Research*, *112*, A09308. https://doi.org/10.1029/2006JA012006
Deng, Y., Lu, G., Kwak, Y.-S., Sutton, E., Forbes, J., & Solomon, S. (2009). Reversed ionospheric convections during the November 2004 storm: Impact on the upper atmosphere. *Journal of Geophysical Research*, *114*, A07313. https://doi.org/10.1029/2008JA013793
Dhadly, M. S., Emmert, J. T., Drob, D. P., Conde, M. G., Doornbos, E., Shepherd, G. G., et al. (2017). Seasonal dependence of geomagnetic active-time northern high-latitude upper thermospheric winds. *Journal of Geophysical Research: Space Physics*, *123*, 739–754. https://doi.org/10.1002/2017JA024715
Dickinson, R. E., Ridley, E., & Roble, R. (1981). A three-dimensional general circulation model of the thermosphere. *Journal of Geophysical Research*, *86*(A3), 1499–1512.
Drob, D. P., Emmert, J. T., Meriwether, J. W., Makela, J. J., Doornbos, E., Conde, M., et al. (2015). An update to the Horizontal Wind Model (HWM): The quiet time thermosphere. *Earth and Space Science*, *2*, 301–319. https://doi.org/10.1002/2014EA000089
Dungey, J. W. (1961). Interplanetary magnetic field and the auroral zones. *Physical Review Letters*, *6*(2), 47–48.
Förster, M., Rentz, S., Köhler, W., Liu, H., & Haaland, S. (2008). IMF dependence of high-latitude thermospheric wind pattern derived from CHAMP cross-track measurements. *Annales Geophysicae*, *26*, 1581–1595. Copernicus GmbH.
Fuller-Rowell, T., & Rees, D. (1984). Interpretation of an anticipated long-lived vortex in the lower thermosphere following simulation of an isolated substorm. *Planetary and space science*, *32*(1), 69–85.
Hapgood, M. (1992). Space physics coordinate transformations: A user guide. *Planetary and Space Science*, *40*(5), 711–717.
Hardy, D. A., Gussenhoven, M., & Holeman, E. (1985). A statistical model of auroral electron precipitation. *Journal of Geophysical Research*, *90*(A5), 4229–4248.
Hardy, D. A., Gussenhoven, M., Raistrick, R., & McNeil, W. (1987). Statistical and functional representations of the pattern of auroral energy flux, number flux, and conductivity. *Journal of Geophysical Research*, *92*(A11), 12,275–12,294.
Huang, Y., Richmond, A. D., Deng, Y., & Roble, R. (2012). Height distribution of Joule heating and its influence on the thermosphere. *Journal of Geophysical Research*, *117*, A08334. https://doi.org/10.1029/2012JA017885
Kamide, Y., & Matsushita, S. (1979). Simulation studies of ionospheric electric fields and currents in relation to field-aligned currents. 1. Quiet periods. *Journal of Geophysical Research*, *84*(A8), 4083–4098.
Killeen, T., Won, Y.-I., Niciejewski, R., & Burns, A. (1995). Upper thermosphere winds and temperatures in the geomagnetic polar cap: Solar cycle, geomagnetic activity, and interplanetary magnetic field dependencies. *Journal of Geophysical Research*, *100*(A11), 21,327–21,342.
Knipp, D., Tobiska, W. K., & Emery, B. (2004). Direct and indirect thermospheric heating sources for solar cycles 21–23. *Solar Physics*, *224*(1), 495–505.
Kosch, M., Cierpka, K., Rietveld, M., Hagfors, T., & Schlegel, K. (2001). High-latitude ground-based observations of the thermospheric ion-drag time constant. *Geophysical Research Letters*, *28*(7), 1395–1398.
Kosch, M., Hagfors, T., & Schlegel, K. (1998). Extrapolating EISCAT Pedersen conductances to other parts of the sky using ground-based TV auroral images. *Annales Geophysicae*, *16*, 583–588.
Kosch, M. J., & Nielsen, E. (1995). Coherent radar estimates of average high-latitude ionospheric Joule heating. *Journal of Geophysical Research*, *100*(A7), 12,201–12,215.
Laundal, K. M., & Richmond, A. D. (2017). Magnetic coordinate systems. *Space Science Reviews*, *206*(1-4), 27–59.
Liu, H., Lühr, H., Watanabe, S., Köhler, W., Henize, V., & Visser, P. (2006). Zonal winds in the equatorial upper thermosphere: Decomposing the solar flux, geomagnetic activity, and seasonal dependencies. *Journal of Geophysical Research*, *111*, A07307. https://doi.org/10.1029/2005JA011415
Lu, G., Baker, D., McPherron, R., Farrugia, C., Lummerzheim, D., Ruohoniemi, J., et al. (1998). Global energy deposition during the January 1997 magnetic cloud event. *Journal of Geophysical Research*, *103*(A6), 11,685–11,694.
Lu, G., Richmond, A., Emery, B., & Roble, R. (1995). Magnetosphere-ionosphere-thermosphere coupling: Effect of neutral winds on energy transfer and field-aligned current. *Journal of Geophysical Research*, *100*(A10), 19,643–19,659.
Lühr, H., Rentz, S., Ritter, P., Liu, H., & Häusler, K. (2007). Average thermospheric wind patterns over the polar regions, as observed by CHAMP. *Annales Geophysicae*, *25*, 1093–1101.
Matsuo, T., Richmond, A. D., & Hensel, K. (2003). High-latitude ionospheric electric field variability and electric potential derived from DE-2 plasma drift measurements: Dependence on IMF and dipole tilt. *Journal of Geophysical Research*, *108*(A1), 1005. https://doi.org/10.1029/2002JA009429
McHarg, M., Chun, F., Knipp, D., Lu, G., Emery, B., & Ridley, A. (2005). High-latitude Joule heating response to IMF inputs. *Journal of Geophysical Research*, *110*, A08309. https://doi.org/10.1029/2004JA010949
Pettigrew, E., Shepherd, S., & Ruohoniemi, J. (2010). Climatological patterns of high-latitude convection in the Northern and Southern Hemispheres: Dipole tilt dependencies and interhemispheric comparisons. *Journal of Geophysical Research*, *115*, A07305. https://doi.org/10.1029/2009JA014956
Rich, F. J., Gussenhoven, M., & Greenspan, M. E. (1987). Using simultaneous particle and field observations on a low-altitude satellite to estimate Joule heat energy flow into the high-latitude ionosphere (Tech. Rep.). MA: Air Force Geophysics Lab. Hanscom AFB.
Richmond, A., & Roble, R. (1987). Electrodynamic effects of thermospheric winds from the ncar thermospheric general circulation model. *Journal of Geophysical Research*, *92*(A11), 12,365–12,376.

Rishbeth, H. (1977). Drifts and winds in the polar *F* region. *Journal of Atmospheric and Terrestrial Physics*, *39*(1), 111–116.
Robinson, R., Vondrak, R., Miller, K., Dabbs, T., & Hardy, D. (1987). On calculating ionospheric conductances from the flux and energy of precipitating electrons. *Journal of Geophysical Research*, *92*(A3), 2565–2569.
Ruohoniemi, J., & Baker, K. (1998). Large-scale imaging of high-latitude convection with Super Dual Auroral Radar Network HF radar observations. *Journal of Geophysical Research*, *103*(A9), 20,797–20,811.
Ruohoniemi, J., & Greenwald, R. (1996). Statistical patterns of high-latitude convection obtained from Goose Bay HF radar observations. *Journal of Geophysical Research*, *101*, 21–743.
Ruohoniemi, J., & Greenwald, R. (2005). Dependencies of high-latitude plasma convection: Consideration of interplanetary magnetic field, seasonal, and universal time factors in statistical patterns. *Journal of Geophysical Research*, *110*, A90204. https://doi.org/10.1029/2004JA010815
Sakanoi, T., Fukunishi, H., Okano, S., Sato, N., Yamagishi, H., & Yukimatu, A. S. (2002). Dynamical coupling of neutrals and ions in the high-latitude *F* region: Simultaneous FPI and HF radar observations at Syowa Station, Antarctica. *Journal of Geophysical Research*, *107*(A11), 1388. https://doi.org/10.1029/2001JA007530
Shepherd, S. (2014). Altitude-adjusted corrected geomagnetic coordinates: Definition and functional approximations. *Journal of Geophysical Research: Space Physics*, *119*, 7501–7521. https://doi.org/10.1002/2014JA020264
Thayer, J. (1998). Height-resolved Joule heating rates in the high-latitude *E* region and the influence of neutral winds. *Journal of Geophysical Research*, *103*(A1), 471–487.
Thayer, J., Vickrey, J., Heelis, R., & Gary, J. (1995). Interpretation and modeling of the high-latitude electromagnetic energy flux. *Journal of Geophysical Research*, *100*(A10), 19,715–19,728.
Thayer, J. P., & Killeen, T. (1993). A kinematic analysis of the high-latitude thermospheric neutral circulation pattern. *Journal of Geophysical Research*, *98*(A7), 11,549–11,565.
Thébault, E., Finlay, C. C., Beggan, C. D., Alken, P., Aubert, J., Barrois, O., et al. (2015). International geomagnetic reference field: The 12th generation. *Earth, Planets and Space*, *67*(1), 79.
Titheridge, J. (1995). Winds in the ionosphere—A review. *Journal of Atmospheric and Terrestrial Physics*, *57*(14), 1681–1714.
Tsuda, T., Nozawa, S., Brekke, A., Ogawa, Y., Motoba, T., Roble, R., & Fujii, R. (2007). An ion drag contribution to the lower thermospheric wind in the summer polar region. *Journal of Geophysical Research*, *112*, A06319. https://doi.org/10.1029/2006JA011785
Tsurutani, B., Mannucci, A., Iijima, B., Abdu, M. A., Sobral, J. H. A., Gonzalez, W., et al. (2004). Global dayside ionospheric uplift and enhancement associated with interplanetary electric fields. *Journal of Geophysical Research*, *109*, A08302. https://doi.org/10.1029/2003JA010342
Vickrey, J. F., Vondrak, R. R., & Matthews, S. J. (1981). The diurnal and latitudinal variation of auroral zone ionospheric conductivity. *Journal of Geophysical Research*, *86*(A1), 65–75.
Wallis, D., & Budzinski, E. E. (1981). Empirical models of height integrated conductivities. *Journal of Geophysical Research*, *86*(A1), 125–137.
Weimer, D. (2005). Improved ionospheric electrodynamic models and application to calculating Joule heating rates. *Journal of Geophysical Research*, *110*, A05306. https://doi.org/10.1029/2004JA010884